Article

Simulation of intercalation and phase transitions in nano-porous, polycrystalline agglomerates

Check for updates

Simon Daubner[1,2] ✉, Marcel Weichel[2], Martin Reder[2,3], Daniel Schneider[2,3], Qi Huang[4], Alexander E. Cohen[5], Martin Z. Bazant[5] & Britta Nestler[2,3]

Optimal microstructure design of battery materials is critical to enhance the performance of batteries for tailored applications such as high power cells. Accurate simulation of the thermodynamics, transport, and electrochemical reaction kinetics in commonly used polycrystalline battery materials remains a challenge. Here, we combine state-of-the-art multiphase field modelling with the smoothed boundary method to accurately simulate complex battery microstructures and multiphase physics. The phase-field method is employed to parameterize complex open pore cathode microstructures and we present a formulation to impose galvanostatic charging conditions on the diffuse boundary representation. By extending the smoothed boundary method to the multiphase-field method, we build a simulation framework which is capable of simulating the coupled effects of intercalation, anisotropic diffusion, and phase transitions in arbitrary complex polycrystalline agglomerates. This method is directly compatible with voxel-based data, e.g., from X-ray tomography. The simulation framework is used to study the reversible phase transitions in Li_xNiO_2 in dense and nanoporous agglomerates. Based on the thermodynamic consistency of phase-field approaches with ab-initio simulations and the open circuit potential, we reconstruct the Gibbs free energies of four individual phases (H1, M, H2 and H3) from experimental cycling data. The results show remarkable agreement with previously published DFT results. From charge simulations, we discover a strong influence of particle morphology on the phase transition behaviour, in particular a shrinking core-like behaviour in dense polycrystalline structures and a particle-by-particle mosaic behavior in nanoporous samples. Overall, the proposed simulation framework enables the detailed study of phase transitions in intercalation materials to enhance microstructure design and fast charging protocols.

The microstructure of electrode materials strongly influences the rate performance of intercalation batteries. In addition to transport of the charge carrier in the electrolyte phase and intercalation reactions at the electrolyte-active material interface, transport within the active material is a critical aspect of battery function. Besides the material-specific crystal structure, ion transport in electrode particles is strongly influenced by the morphology (structural appearance of crystalline materials on the mesoscopic scale). Layered-oxides based on nickel, manganese and cobalt (NMC) are state-of-the art cathode materials for commercial lithium-ion cells in high-capacity applications such as electric vehicles. Typically, NMCs form hierarchical structures of many primary crystals agglomerated in a spherical secondary particle (see Fig. 1c–e), sometimes referred to as meatball structure[1,2]. Similar secondary morphologies can be obtained for the P2-type $Na_xNi_{1/4}Mn_{3/4}O_2$ which is a promising cathode material for sodium ion batteries[3]. Ionic transport can be altered in polycrystalline materials through microstructure design such as tailoring crystallographic orientations[4] or introducing nano-porosity as in Fig. 1d)[5].

[1]Dyson School of Design Engineering, Imperial College London, London, UK. [2]Institute for Applied Materials (IAM-MMS), Karlsruhe Institute of Technology, Karlsruhe, Germany. [3]Institute for Digital Materials Science (IDM), Karlsruhe University of Applied Sciences, Karlsruhe, Germany. [4]State Key Lab of Powder Metallurgy, Central South University, Changsha, China. [5]Department of Chemical Engineering, Massachusetts Institute of Technology, Cambridge, USA. ✉e-mail: s.daubner@imperial.ac.uk

$$\tilde{\mu}_{Li+}^{A} = \tilde{\mu}_{Li+}^{elyte} \qquad \eta = (\tilde{\mu}_{Li+}^{elyte} - \tilde{\mu}_{Li+,surf}^{C})/e$$
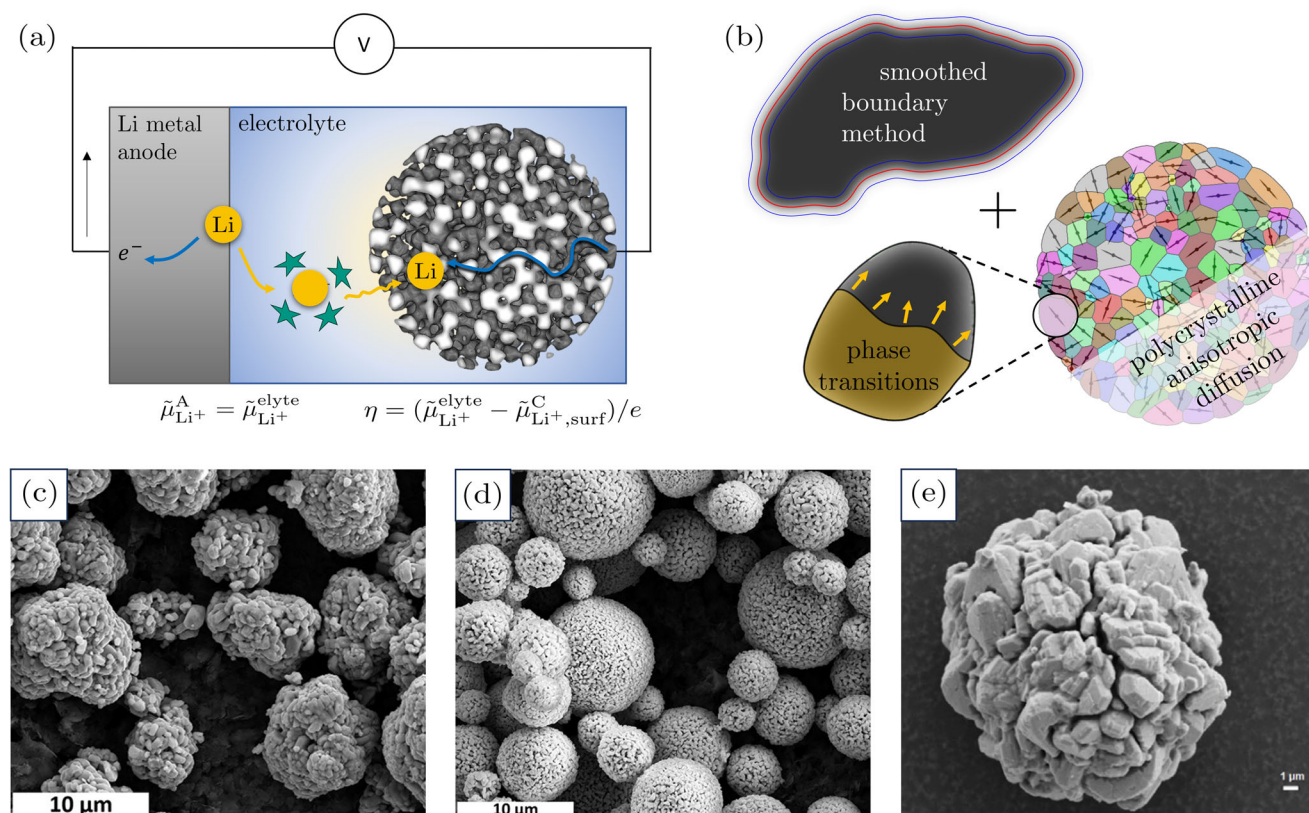
Fig. 1 | Modelling nanoporous, polycrystalline agglomerates. a Nanoporous $Li_{X}TMO_{2}$ cathode particle in half-cell configuration. **b** The model combines the smoothed boundary method to parametrize the interface between electrolyte and active material with the multiphase-field approach to model anisotropic diffusion in polycrystalline agglomerates coupled with phase transitions. Secondary particle morphologies of (**c**) as-prepared NCM111 and (**d**) nano-porous NMC111 after spraydrying reproduced from Müller et al.[5] published under a CC BY-NC-ND licence. The $Na_{X}Ni_{1/4}Mn_{3/4}O_{2}$ particle shown in (**e**) is reproduced from Pfeiffer et al.[3] and has been published under the CC BY licence.

Mesoscale simulations are essential for understanding the structure-property relationship between agglomerate microstructure and the effective rate performance, which is crucial for designing materials for battery applications[6]. Furthermore, reversible phase transformations during cycling are a common phenomenon in intercalation compounds including lithium iron phosphate (LFP), $LiNiO_{2}$ and many sodium intercalation materials[3,7–11]. The nature of these materials can only be modelled and understood if phase transformations are accounted for which is typically done using phase-field methods[12,13]. Ideally, meso-scale simulations need to cover the electro-chemical intercalation reaction on complex three-dimensional surfaces as well as the diffusion and coupled phase transformations within the polycrystalline active material.

The parametrization of a complex microstructure, such as polycrystallinity and porosity, in mesoscale simulations poses a challenge which can be addressed in two ways. First, the interfaces between electrolyte, active material and individual grains can be discretized with a boundary-conforming mesh e.g. finite elements where the nodes are located on the boundary. This approach relies on powerful meshing algorithms as the quality of the 'worst element' will determine the overall stability of the simulation. If the domain boundary evolves over time, mesh moving algorithms can be employed leading to an arbitrary Lagrangian-Eulerian framework[14]. However, large changes of the geometry may lead to large mesh distortion and a costly re-meshing becomes necessary. Another option to parametrize the geometry is the use of a phase-field variable or indicator function, ψ, which distinguishes between electrolyte ($\psi = 0$) and active material ($\psi = 1$). The phase boundary is approximated by a diffuse but steep transition region, where ψ takes values between 0 and 1, which thus becomes a regularized indicator function representing a local volume fraction of the active material. It can be shown that for $\psi \in [0, 1]$ the isoline given by $\psi = 0.5$ corresponds to the sharp boundary problem. Therefore, the geometry is implicitly parametrized via the phase variable and the spatial discretization can be performed independently of the microstructure. In the context of battery materials, the phase-field approach comes with some additional benefits: It is desirable to perform simulations based on microscopy data which is typically obtained as pixelated images. In the case of FIB-SEM measurements three-dimensional voxel data is obtained through slicing and imaging[15,16]. From an implementation perspective, regular grids combined with a finite difference discretization are straightforward to implement and simulations can be accelerated using massive parallelization on GPUs[17]. Employing the pixel (or voxel) grid from microscopy image data for the simulation of concentration evolution allows for direct comparison of simulations with in-situ experiments.

If the regularized indicator function does not evolve but is simply used to solve partial differential equations (PDEs) with boundary conditions on arbitrarily shaped geometries, this approach has also been termed *smoothed boundary method* (SBM)[18,19]. The SBM has been introduced in the work of Kockelkoren et al.[20] and was successfully used in subsequent works[18,21]. A detailed discussion of various ways to impose boundary conditions on the diffuse domain boundary can be found in[22], where the SBM is also discussed in comparison with similar approaches like level-set, the immersed interface method or the ghost fluid method. In most works, the smooth transition is imposed by a tanh-function[20,22] which is also the 1D equilibrium solution of a phase-field functional based on a double-well potential[21]. Alternatively, the obstacle potential can be employed[23]. The SBM has been employed to study battery microstructure at both the particle and electrode level. The formulation is used to couple the intercalation reaction on a complex electrode surface with solid-state diffusion in the active material. Many works assume Fickian diffusion and no phase evolution[24–26]. Other works cover phase

transitions in a single particle described by the Cahn-Hilliard model, some of them assuming purely diffusion-driven kinetics[27,28], some including elastic contributions[29,30]. The recent work by Qu et al. extends the Cahn-Hilliard model for phase transitions in graphite on a complex porous electrode microstructure[31]. However, a model formulation which allows for detailed investigations of polycrystalline microstructures including material anisotropy, phase transitions and an electrochemical surface reaction on arbitrary complex morphologies is missing in the literature.

This work combines recent advances in the simulation of battery materials with state-of-the-art multiphase field modelling and the smoothed boundary method. The simulation framework is formulated as a single particle model[32] to relate the rich interplay of the insertion reaction, concentration gradients and phase transitions with a global current and voltage response. The underlying assumptions are fast electronic conduction, fast reaction kinetics at the lithium metal anode and fast ion transport inside the electrolyte as sketched in Fig. 1a. The multiphase-field method is a highly versatile tool to study intercalation and diffusion in polycrystalline systems[6,13] and materials with multiple phase transformations[33,34]. We combine the SBM and the multiphase-field method, stemming from different fields within the phase-field community, to formulate the extended multi-phase smoothed boundary method (MP-SBM). Starting from analytical considerations the methodology is validated and subsequently applied to nano-porous agglomerates of lithium layered oxides LiTMO$_2$.

Results

Multi-phase smoothed boundary method

Typically, the SBM is introduced by modifying all underlying PDEs with the indicator function ψ as outlined in the section "Smoothed boundary method". In the case of a phase transition given by Eq. (9) this would result in a problem definition as illustrated in Fig. 2a. For a multi-phase system with N phases, this also means modifying all N equations given by Eq. (10) together with all PDEs for the coupled multi-physics (mass conservation, mechanics, …) which is a massive interference with the original model and the corresponding simulation code. To utilize existing simulation frameworks like Pace3D[35] or MOOSE[36], we seek to deploy the multiphase-field framework "as is" while only modifying the mass conservation equation for the scope of this work.

The two representations given in Fig. 2 are related by the following considerations. Within the multiphase-field method, the phase-fields $\{\phi_{\text{elyte}}, \phi_\alpha, \ldots\phi_N\}$ denote volume fractions and, therefore, must fulfill the Gibbs simplex constraint, i.e., $\sum_{i=1}^N \phi_i = 1$ and $0\leq\phi_i$ for all phases. The electrolyte region is parametrized by $\phi_{\text{elyte}} = 1 - \psi$ while the active material is given by $\phi_\alpha + \phi_\beta = \psi$. Furthermore, the following relation between volume fractions holds

$$\phi_\alpha = \frac{V_\alpha}{V} = \frac{V_\alpha}{V_{\text{active}}} \frac{V_{\text{active}}}{V} = \varphi\psi \quad \text{and thus} \quad \frac{\partial \phi_\alpha}{\partial t} = \psi\frac{\partial \varphi}{\partial t} \quad (1)$$

We employ the multiphase-field evolution equations given by Eq. (10) and, to preserve the shape of the active material, all pairwise phase mobilities $M_{\text{elyte},\alpha}$ can be set to zero which results in $\partial\phi_{\text{elyte}}/\partial t = 0$.

Through the analytical comparison of the two approaches sketched in Fig. 2 (see detailed derivation of evolution equations in Supplementary

Results) the modified evolution equation for the chemical potential reads

$$\frac{\partial \mu}{\partial t} = \left[\sum_{\alpha=A}^N \frac{\partial c^\alpha}{\partial \mu}\phi_\alpha\right]^{-1}\left[\nabla\cdot\left(\left(\sum_{\alpha=A}^N \mathbb{D}^\alpha \frac{\partial c^\alpha}{\partial \mu}\phi_\alpha\right)\nabla\mu\right)\right.$$
$$\left. +|\nabla\psi|j_N + \psi R_{\text{bulk}} - \sum_{\alpha=A}^N c^\alpha \frac{\partial\phi_\alpha}{\partial t}\right] \quad (2)$$

where μ is the chemical potential, c^α is the phase-specific lithium concentration, $\mathbb{D}^\alpha$ is the anisotropic diffusion tensor of phase α and j_N denotes the local intercalation flux. Note that for the generalized multiphase system with N phases we have introduced the two subsets of inactive material $\phi_0 = \sum_{\alpha=0}^{A-1} \phi_\alpha$ and active material $\psi = \sum_{\alpha=A}^N \phi_\alpha$. In the case of one electrolyte phase and $N - 1$ active phases, the expressions simplify to $\phi_0 = \phi_{\text{elyte}}$ and $\psi = 1 - \phi_{\text{elyte}}$. The averaged concentration in the active material is then given as $c_{\text{active}} = (\sum_{\alpha=A}^N c^\alpha\phi_\alpha)/\psi$.

The proposed modification is directly compatible with previous multiphase-field works and, thus, allows for the direct inclusion of anisotropic diffusion in polycrystalline NMC agglomerates[6] and phase transitions of the lithium layered oxide during intercalation[34]. Furthermore, the new approach is directly applicable to voxel-based segmented image data (see Fig. 3a, b) and is able to apply boundary conditions on arbitrary particle morphologies (Fig. 3c) to simulate constant current - constant voltage (CC-CV) charging protocols or other dynamic loads.

Phase transitions in layered oxides

As discussed in the introduction, many cathode materials undergo reversible phase transformations during cycling (LFP, LNO and many sodium compounds). The Ni layered oxide LiNiO$_2$ transitions from a hexagonal (H) to monoclinic (M) crystal structure at various stages of lithium content denoted as H1, H2, H3 and M phase[8,9]. The phase transformation to H3 at a low lithium filling fraction is the most limiting factor in the practical applicability of LiNiO$_2$ for multiple reasons: The phase transition at high potentials poses a kinetic limitation at high charging rates. Additionally, the lattice mismatch of the H2- and H3-phase can lead to mechanical stress which contributes to degradation[9,37]. Lastly, LiNiO$_2$ suffers from oxygen release and an associated irreversible phase transition to disordered spinel-like/rock-salt-like structures, especially at surfaces exposed to the electrolyte[38,39]. The gas release is strongly pronounced at high potentials in the H2 and H3 phase[9].

Modelling all these coupled effects poses a severe challenge. Progress has been made on individual aspects such as the thermodynamic modelling of surface degradation[40]. For the scope of this work we focus on reversible phase transformations and their influence on rate performance. To this end we utilize the thermodynamic framework discussed by Daubner et al.[34] which relates the chemical Gibbs free energy used in phase-field models to experimentally measured open circuit potential (V_{OC}) data. In the context of intercalation materials it is favourable to formulate the chemical free energies and evolutions equations in terms of the local lithium site filling fraction $x^\alpha = c^\alpha/c_{\text{ref}}$ where we use the concentration in the fully lithiated state as a reference. From the lattice parameters reported in[9], we infer $c_{\text{ref}} = 48967$ mol/m^3. The average site filling fraction X in the cathode active material volume V is then given as $X = (\int x dV)/V$. As the system strives to minimize its

Fig. 2 | Two possible representations of the triple phase problem. In the diffuse boundary approach (**a**) the regularized indicator function ψ parametrizes the active material and does not evolve. The order parameter φ distinguishes high- and low-concentration phases and evolves within the whole computational domain. The multi-phase field approach (**b**) employs three volume fractions ϕ_α, ϕ_β and ϕ_{elyte} which fulfill the sum constraint $\sum_0^N \phi_i = 1$.
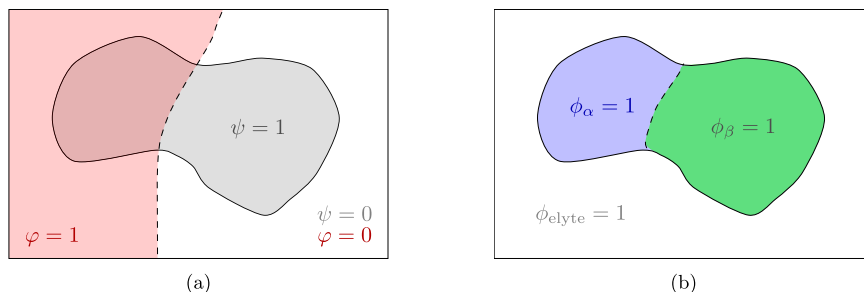
Fig. 3 | Multi-phase smoothed boundary method.
a Starting from labelled microscopy data the (**b**)
phase-fields ϕ_i can be defined. The spatial overlap of
phase-fields within the diffuse transition region is
illustrated by the blending of RGB values. **c** The
interface between electrolyte and active material is
then implicitly defined by $|\nabla\phi_{\text{elyte}}|$.
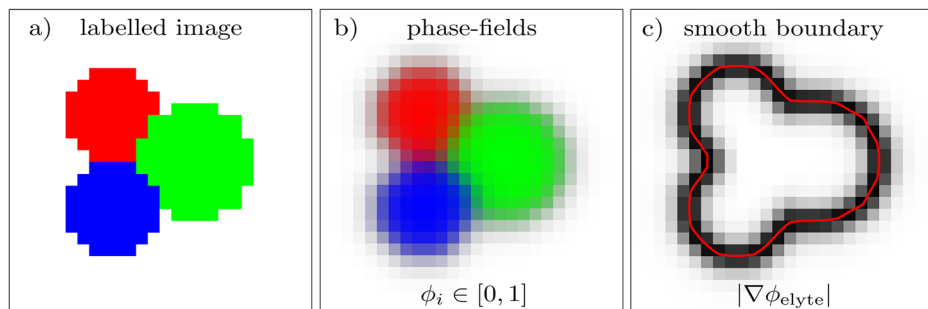
**Fig. 4 | V_{OC} and derived Gibbs free energies for
Li_XNiO_2.** Chemical potential fits to the measured
V_{OC} using Eq. (4) shown in (**a**) which results in the
free energy landscape shown in (**b**). Gray datapoints
in (**a**) correspond to experimental voltage data for
Li_XNiO_2 obtained at $C/10$[9] and in (**b**) to the convex
hull from DFT-based cluster expansion[37]. Gray
shaded areas mark the single phase regions observed
in Li_XNiO_2.
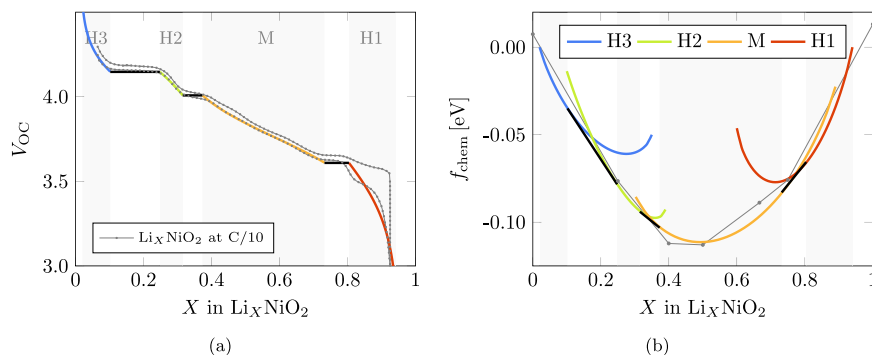
energy, new phases nucleate and a two-phase coexistence can be observed
which corresponds to a plateau in the V_{OC}. Within the multiphase-field
framework described in the section "Multiphase-field formulation" the
functions to express the chemical energy of lithium in the host structure
must be invertible (to express x^α as a function of chemical potential μ) which
is fulfilled e.g by a logarithmic fit

$$f^\alpha_{\text{chem}} = \mu_0^\alpha x^\alpha + K^\alpha\left[(x^\alpha - x^\alpha_{\text{min}})\ln(x^\alpha - x^\alpha_{\text{min}})\right.$$
$$\left. + (x^\alpha_{\text{max}} - x^\alpha)\ln(x^\alpha_{\text{max}} - x^\alpha)\right] + B^\alpha, \tag{3}$$

$$\mu = \mu_0^\alpha + K^\alpha\left[\ln(x^\alpha - x^\alpha_{\text{min}}) - \ln(x^\alpha_{\text{max}} - x^\alpha)\right]. \tag{4}$$

Consequently, the chemical energetic landscape is approximated by phase-
wise fitting functions f^α_{chem} for the given phases α = H1, M, H2 and H3. In
thermodynamic equilibrium, Gibbs free energies derived from DFT
simulations are consistent with the measured open circuit voltage V_{OC}[34]
which in turn means that the chemical energies can be estimated based on
V_{OC} data. We utilize the data from the third discharge of Li_XNiO_2 at C/10
from De Biasi et al.[9] and fit the expression in Eq. (4) to the data points in
single phase regions as marked by the gray shaded areas in Fig. 4 a). We then
estimate the integration constants B^α in Eq. (3) through the constraint that,
firstly, the phase chemical potentials in the two-phase regions must be equal
(corresponding to the black common tangent in Fig. 4 b) and the voltage
plateaus in Fig. 4 a). Secondly, the end points of the chemical energies over
the lithium fraction range $X \in [0.015, 0.95]$ should be equal to zero such that
the Gibbs free energies are comparable to formation energies and the convex
hull calculated with DFT-based cluster expansion[37]. The whole fitting
procedure has been performed using the *curve_fit* function from the scipy
package and can be found in the corresponding code repository[41].

The function fits displayed in Fig. 4a match the experimental data very
closely which is not surprising given that the discharge data has been used
for fitting. The strongest deviation is observed in the H1 phase ($X \in [0.8,
0.95]$) where the experimentally measured charge and discharge voltage
differ significantly which could be caused by irreversible processes or a
strong asymmetry of battery kinetics even at such low rates as C/10. Detailed
function parameters can be found in the supplementary code[41]. The con-
straint of $f_{\text{chem}}(X = 0.015) = f_{\text{chem}}(X = 0.95) = 0$ results in a reference voltage

of $V_{\text{ref}} = 3.85$ such that the open circuit voltage is given by $V_{\text{OC}} = V_{\text{ref}} - \mu/e$.
The close match of the extrapolated Gibbs free energies with the data points
from the cluster-expanded convex hull[37] is remarkable given that no prior
knowledge about the energy landscape was involved in the fitting procedure.
These results underline the thermodynamic consistency of the chosen
approach in line with the results in[34].

Rate performance of dense vs nanoporous agglomerates

The diffusion in layered oxides is highly anisotropic as the lithium transport
is mainly limited to the space between transition metal oxide layers while
transport across layers can be mediated through crystal defects but is still
orders of magnitude slower. The experiments with LiCoO_2 thin films by
Bouwman et al.[42] show a difference of at least 4-5 orders of magnitude for the
chemical diffusion coefficients for the in-plane and out-of-plane direction
from which we infer that the diffusion across layers is negligibly small ($D_\perp =
0$). We investigate dense and nanoporous polycrystalline agglomerates
inspired by the morphologies shown in Fig. 1c–e. The grains are created
using Voronoi tesselations based on random seeds within a spherical
domain. Using the multiphase-field evolution Eq. (10) without a chemical
driving force ($\Delta f^{\alpha\beta}_{\text{chem}} = 0$), we let the grains evolve driven by curvature
minimization to generate more realistic grain morphologies and create a
diffuse transition region between the electrolyte domain and the active
material as sketched in Fig. 3. All secondary particles in this study are
assumed to have an outer diameter of 5 μm. A random orientation (given by
Euler angles ξ, θ, ζ) is assigned to every grain such that the diffusion tensor of
all possible sub-phases (H1, M, H2, H3) in a grain is given by a rotation from
the material (1-2-3) to the reference coordinate system (x-y-z) as described
in[6]

$$\mathbb{D}^\alpha_{xyz} = \mathbb{R}^\alpha(\xi, \theta, \zeta)\,\mathbb{D}_{123}\,(\mathbb{R}^\alpha(\xi, \theta, \zeta))^T, \quad \mathbb{D}_{123} = \begin{bmatrix} D_\| & 0 & 0 \\ 0 & D_\| & 0 \\ 0 & 0 & D_\perp \end{bmatrix}.$$

The in-plane diffusivity is assumed to have a constant value of $D_\| =
10^{-10}$ cm^2/s[6]. The energetic barrier for intercalation is given by the standard
exchange current density $j_{00} = Fk_0 c_{\text{max}} \approx 1.2$ A m^{-2} which has been fitted

Fig. 5 | Charge simulations of dense and nano-porous agglomerates for rates of $C \in [0.1, 1, 2, 4]$. The charge behaviour of NMC811 (**a, b**) is compared to LNO including three phase transitions (**c, d**). The left column displays results obtained for a dense poylcrystalline structure while the agglomerate with open nanoporosity is shown on the right. Black dashed lines represent the equilibrium voltage fits.
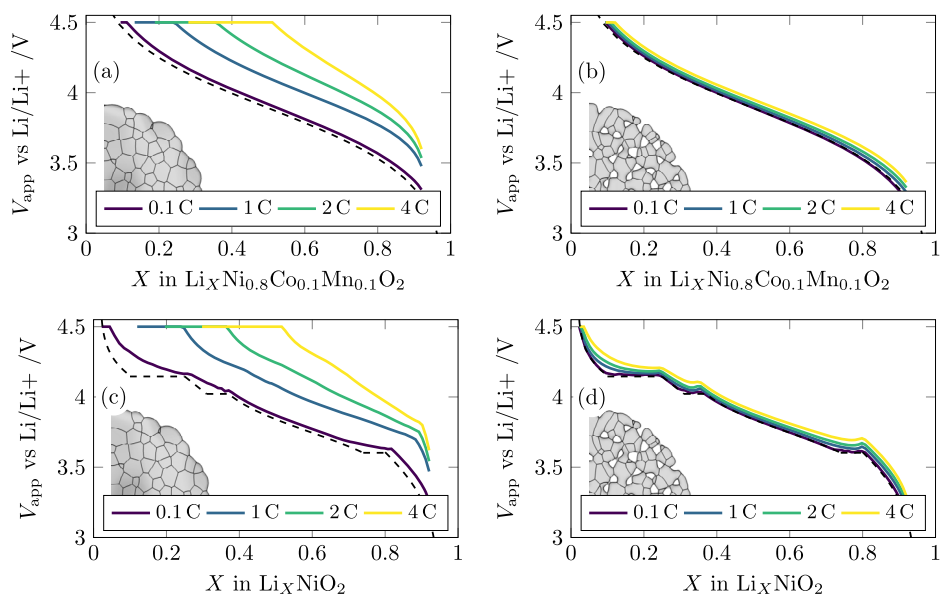
using coupled ion-electron transfer kinetics[43] as described in Section "Electro-chemical boundary condition" based on the data provided in the Supplementary materials Figure S22 in[44]. Note that this factor is rather high compared to other values found in literature[45] which can be explained by the choice of 1M LiClO$_4$ in ECM:DC as electrolyte while values for LiPF$_6$ tend to be smaller by a factor of 2–5[44]. The pairwise interfacial energies are set to $\gamma_{\alpha\beta}$ = 0.1 J/m^2 [34] and the effect of coherency strain is not considered in the following. A summary of simulation input parameters can be found in the Supplementary Note 2.

In Fig. 5 we compare the voltages for a dense vs nanoporous agglomerate (see inset pictures) subject to a CC-CV charging protocol with C = [0.1, 1, 2, 4] [1/h] until the upper cut-off voltage is reached.

To decouple the influence of phase transitions on the applied voltage we also simulate the charge of solid-solution NMC811 based on the fitted free energy and V_{OC} in[6] as a reference. Generally, a higher charging rate leads to a higher overpotential, i.e. the applied voltage deviates stronger from the thermodynamic equilibrium voltage V_{OC}. As a result, the upper cut-off voltage of 4.5 V is reached at a lower average concentration of lithium X inside the active material which can be mainly attributed to diffusion limitation. The dense agglomerate structure is controlled by diffusion from the outer surface towards the center of the particle. The misorientation of grains coupled with the strong diffusion anisotropy leads to tortuous pathways inside the polycrystal which additionally hinders the lithium transport. In the case of LNO, the rate performance is strongly influenced by the shrinking core-like phase transitions inside the agglomerate. The nanoporosity leads to a strong decrease of diffusion overpotentials (see Fig. 5b, d) due to the faster transport of lithium in the electrolyte phase. Furthermore, the influence of anisotropy becomes weaker as more grains can be accessed through kinetically favourable facets and are less restricted by neighbouring grains. The rate performance of both materials increases such that even a 4 C charge becomes feasible without notable increase of overpotentials.

To better understand the phase transitions in LNO, we exemplarily show the temporal evolution of local concentrations for a 1 C charge in Fig. 6. The morphology of the agglomerate strongly influences the observed phase transitions behaviour. As the dense particle is limited by diffusion from the outer surface towards the center, the evolution of phases follows the concentration gradient and, thus, can be described by a shrinking core-type behaviour. Due to diffusion anisotropy, there are preferred sites for the nucleation of the next phase and the shrinking core is not rotational symmetric. Towards the end of discharge, the M-phase can be found in the middle of the particle (green) while H2 (light blue) and H3 (dark blue) form rings in radial direction. The nanoporous agglomerate shows a stronger

influence of the surface reaction rate and phase nucleation. The availability of many surface sites leads to a nucleation of new phases at energetically favourable sites inside the agglomerate which are predominantly triple/higher-order junctions and grain features with a high curvature. This behaviour leads to the grain-by-grain mosaic of phase transitions observed in the bottom row of Fig. 6.

Discussion

The complex morphology of polycrystalline secondary particles has a strong influence on the overall battery rate performance. This effect is even more pronounced in the case of intercalation materials undergoing phase transitions such as the lithium layered oxide LiNiO$_2$ (LNO). The derivations in Section "Multi-phase smoothed boundary method" underline that the multi-phase smoothed boundary method (MP-SBM) is a straight-forward extension of standard multi-phase field methods and can be implemented utilizing existing code frameworks such as PACE3D or MOOSE. The proposed framework is also transferable to multi order parameter models[46,47] without further modification. Thus, the proposed methodology leverages existing software with only minor modifications to the mass conservation equation and the intercalation reaction.

The observed particle mosaic in nanoporous LNO represents one of the central predictions of our simulation study. While this phenomenon has not yet been experimentally confirmed, several lines of evidence support our findings:

- The rate capability experiments performed by Müller et al.[5] for dense and nano-porous NMC111 particles show a significant difference in discharge capacities for varying C-rates. This result is consistent with the simulation results depicted in Fig. 5. It should be noted that these measurements utilized pouch cells with cathode thicknesses of $\approx$ 100 μm, indicating that electrode porosity and tortuosity likely affect charge kinetics at high rates which is not considered in our current simulation study.
- Significant state-of-charge heterogeneities have been observed in secondary agglomerates of NMC111 and NMC532, even under slow charging conditions and extended relaxation times[48,49]. The lithiation proceeds from the particle surface towards the center but is also influenced by anisotropy, cracks and pores inside the agglomerate[48,49].
- A shrinking core behaviour has been observed for large ($\approx$ 10 μm diameter) dense particles of the biphasic LFP cathode material[50].
- The transition from a shrinking core-type to a wave-like phase transition as a function of particle size and diffusivity has been discussed by Fraggedakis et al.[51] for LCO, LFP and graphite.
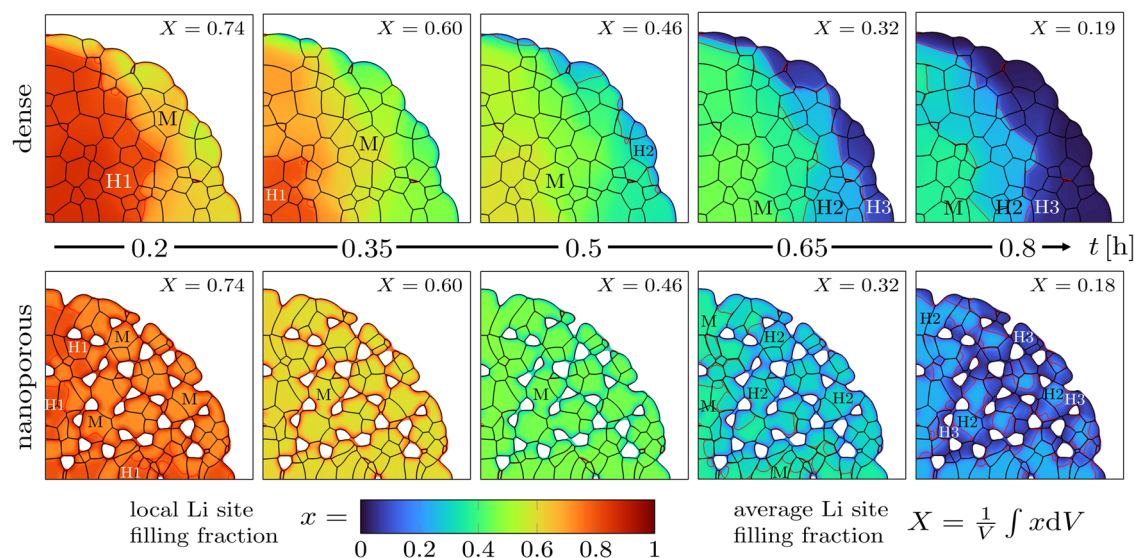
Fig. 6 | Evolution of Li concentration and phases during 1C CC-CV charge. Top row shows a dense agglomerate where concentration gradients form in the radial direction and the phase transitions follow a shrinking core behaviour. The nanoporous agglomerate in the bottom row exhibits a more homogenous lithium distribution and follows a mosaic pattern during the phase transition. Patches of each phase have been labelled for reference.

Fig. 7 | 3-dimensional delithiation simulation of polycrystalline LNO agglomerate at 1C. Cut-out yields insight into the lithium distribution and phase transformations inside the particle. Grain boundaries between primary crystals are indicated by gray lines.
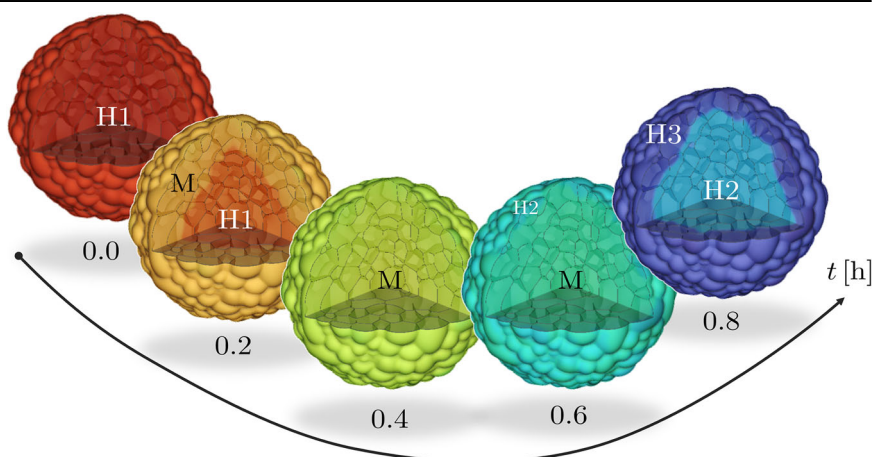
- The mosaic pattern of high- and low-concentration phases identified in nanoporous simulations closely resembles previous observations made for ensembles of nano-sized (100–500 nm) LFP single crystals. They typically exhibit a particle-by-particle phase transition pathway during charging, with the majority being either fully lithiated or fully delithiated, and only $\approx$ 2 % actively transitioning at any given time[52]. This active population varies with the charging rate, transitioning from sequential particle-by-particle behaviour at low rates to concurrent intercalation at higher rates[53]. Such behaviour is caused by the interplay of intercalation fluxes and the energetic barrier to nucleate a new phase inside a particle or grain which seems to be a general feature of phase transforming battery materials.

Thus, our simulation outcomes for LNO are consistent with documented behaviors of other intercalation materials undergoing phase transitions, including the extensively studied LFP system. Our modelling approach also enables the study of pulse-induced activation which has been recently discovered for the phase transformation in LFP[54]. Therefore, the proposed simulation framework not only opens avenues for agglomerate microstructure design but also the optimization of charge protocols for the fast charging of battery materials with phase transitions.

The extension to 3D structures is straightforward as shown in Fig. 7. The voxel-based discretization employed in this work allows for a direct coupling with agglomerate morphologies obtained from X-ray tomography or FIB-SEM.

The current simulation study is limited by the assumption of perfectly reversible phase transitions neglecting the effect of transformation strains and other degradation mechanisms. As discussed in Section "Phase transitions in layered oxides", LNO suffers from irreversible surface degradation, which will be the subject of future studies. The incorporation of coherency strains, oxygen loss, and surface rock-salt formation into the presented multi-phase smoothed boundary framework would allow for the comprehensive study of LNO degradation under realistic cycling conditions. Other limitations at high charging rates are the assumptions of charge neutrality and quasi-equilibrium in the electrolyte phase. In porous agglomerates, the confinement of nanopores could potentially lead to local space charges and lithium depletion in the electrolyte inside the particle which are currently neglected. However, the simulation of lithium migration inside the

electrolyte based on concentrated solution theory[55] adds computational complexity and the challenge of different timescales for lithium transport.

In summary, we proposed the MP-SBM simulation framework to study the coupled effects of intercalation, anisotropic diffusion and phase transitions in arbitrary complex microstructures. We then present a procedure to obtain the chemical free energies from experimental cycling data close to thermodynamic equilibrium which allows us to study the reversible phase transitions in Li_xNiO_2 for the first time. The comparison of simulated charging in dense and nanoporous polycrystalline agglomerates yields insight into the limiting factors for fast charging of such materials.

Methods
Smoothed boundary method
This approach has been successfully used for the simulation of biological cells[19,20], battery materials[27–30] and it has been described in a general sense including Dirichlet as well as Neumann boundary conditions[22]. The framework is general for solving PDEs with boundary conditions imposed on arbitrarily shaped boundaries[19]. The indicator function $\psi \in [0, 1]$ is used to modify the original differential equations such that the boundary conditions are imposed on the diffuse transition region where $\nabla \psi \neq 0$. Following the procedure in[19], we re-write the diffusion-reaction equation for the concentration c with the indicator function ψ as

$$\psi \frac{\partial c}{\partial t} = \nabla \cdot (\psi \mathbb{M}(c) \nabla \mu) + \psi R_{\text{bulk}} + \text{BCs} . \quad (5)$$

$\mathbb{M}$ denotes the chemical mobility tensor which can be anisotropic and a function of concentration while μ denotes the (electro-)chemical potential. Depending on the type of boundary condition, other terms enter the PDE, namely for

$$\text{Dirichlet BC}: \quad \text{PDE} - \frac{1}{\psi} M(\nabla \psi \cdot \nabla(\psi \mu) - |\nabla \psi|^2 \mu_0) \quad (6)$$

$$\text{Neumann BC}: \quad \text{PDE} + |\nabla \psi| j_N \quad (7)$$

where μ_0 is the prescribed (electro-)chemical potential on the Dirichlet boundary, j_N is the normal boundary flux and $j_N = 0$ for a closed system. Both values can vary spatially and/or temporally. Note that Eq. (5) was derived under the assumption of $\nabla \psi \cdot \nabla c = 0$ which means concentration gradients will form 90° angles with the boundary. This assumption could be replaced by another contact angle BC[22].

Multiphase-field formulation
The motion of an interface between high- and low-concentration phases is driven by capillary and chemical forces. For a two-phase interface, the velocity is given by[56,57]

$$v_n = M_0(\Delta f^{\alpha\beta}_{\text{chem}} + \gamma \kappa) \quad (8)$$

where M_0 is the mobility of the phase boundary, γ denotes the interfacial energy and κ the curvature. The driving force $\Delta f^{\alpha\beta}_{\text{chem}} = \mu(c^\alpha - c^\beta) - f^\alpha_{\text{chem}} + f^\beta_{\text{chem}}$ is defined by the difference of grand-chemical potentials. The phase-field method approximates this moving-boundary problem through diffuse interfaces which effectively regularizes the singularity and yields

$$\frac{\partial \phi_\alpha}{\partial t} = M_{\alpha\beta} \left(|\nabla \phi_\alpha| \Delta f^{\alpha\beta}_{\text{chem}} - \gamma \left(\frac{8}{\pi^2 \epsilon^2}(1 - 2\phi_\alpha) - \nabla^2 \phi_\alpha \right) \right) \quad (9)$$

for the two-phase case. The numerical parameter ϵ has been introduced to scale the width of the diffuse interface. Note that the prefactor $|\nabla \phi_\alpha|$ effectively distributes the driving force across a small volumetric region given by the diffuse transition of the phase-field ϕ_α similarly to the treatment of flux boundary conditions in the smoothed boundary method. The gradient norm can be approximated as $|\nabla \phi_\alpha| \approx \frac{4}{\epsilon\pi} \sqrt{\phi_\alpha(1 - \phi_\alpha)}$ for the

obstacle potential which is computationally beneficial. Hence, the phase evolution can be expressed more generally for a multi-phase system as[57]

$$\frac{\partial \phi_\alpha}{\partial t} = \sum_{\beta \neq \alpha}^{\tilde{N}} M_{\alpha\beta} \left(\frac{4}{\epsilon\pi} \sqrt{\phi_\alpha \phi_\beta} \Delta f^{\alpha\beta}_{\text{chem}} - \gamma_{\alpha\beta} K_{\alpha\beta} + J_{\alpha\beta} \right) + \frac{\partial \chi}{\partial \phi_\alpha} \quad (10)$$

where the curvature term $K_{\alpha\beta}$ and additional junction forces $J_{\alpha\beta}$ are given by

$$K_{\alpha\beta} = \frac{1}{\tilde{N}} \left[\nabla^2 \phi_\beta - \nabla^2 \phi_\alpha + \frac{16}{\epsilon^2 \pi^2} \left(\phi_\beta - \phi_\alpha \right) \right], \quad (11)$$

$$J_{\alpha\beta} = \frac{1}{\tilde{N}} \sum_{\gamma \neq \beta \neq \alpha}^{N} (\gamma_{\beta\gamma} - \gamma_{\alpha\gamma}) \left(\nabla^2 \phi_\gamma + \frac{16}{\epsilon^2 \pi^2} \phi_\gamma \right). \quad (12)$$

The term χ adds noise to enable heterogeneous nucleation of new phases and is explained in more detail in the Supplementary Note 1. Due to the length scale of the problem, we assume local quasi-equilibrium of chemical potentials within diffuse interface regions $\mu_\alpha = \mu_\beta = \mu$. This is motivated by the fact that grain boundaries are on the length scale of ≈ 10 nm while the pixel resolution of FIB-SEM or nanoCT imaging for battery materials is on the scale of $20-100$ nm. Employing this constraint together with the definition of the phase averaged concentration $c = \sum c_\alpha \phi_\alpha$ allows for a reformulation of the mass balance in terms of an evolution of chemical potential[58,59]

$$\frac{\partial \mu}{\partial t} = \left[\sum_\alpha^N \frac{\partial c^\alpha}{\partial \mu} \phi_\alpha \right]^{-1} \left(\nabla \cdot (\mathbb{M} \nabla \mu) + R_{\text{bulk}} - \sum_\alpha^N c^\alpha \frac{\partial \phi_\alpha}{\partial t} \right). \quad (13)$$

Note that the chemical mobility tensor is given by the weighted sum of phase-specific diffusivities and thermodynamic factors $\mathbb{M} = \sum \mathbb{D}^\alpha (\partial c^\alpha / \partial \mu) \phi_\alpha$. This approach is computationally beneficial compared to solving N coupled PDEs for the phase-specific concentrations c_α. We assume that there is no bulk reaction term for intercalated species while the electro-chemical surface reaction will later be introduced via the smoothed boundary method. The full set of equations can be derived starting from a free energy functional as given in the Supporting information of Daubner et al.[34].

Electro-chemical boundary condition
The intercalation reaction is modelled employing coupled ion-electron transfer (CIET) theory, which unifies Marcus kinetics of electron transfer with Butler-Volmer kinetics of ion transfer[43]. Assuming symmetry of the reaction ($\alpha = 0.5$) and that the ion transfer step is rate limiting, the intercalation current on the surface between electrolyte and active material is given by[43,44]

$$j_N = 2Fk_0 \sqrt{c} (c_{\text{max}} - c) \sinh \left(\frac{e}{2k_B T}(V^\ominus_{\text{cell}} - V) - \frac{\mu_{\text{surf}}}{2k_B T} \right) \quad (14)$$

where F is the Faraday constant, k_B the Boltzmann constant, T denotes absolute temperature and e is the elementary charge. The reaction rate constant k_0 is a lumped parameter comprising contributions from the reorganization and ion transfer energies, the activity of Li^+ in the electrolyte and a quantum mechanical prefactor[43]. $V^\ominus_{\text{cell}}$ denotes a reference cell voltage and V the applied voltage between the two electrodes under the assumption of fast reaction on the anode side[34]. The assumption of galvanostatic (dis-)charge is fulfilled by restricting the total current I

$$I = \int_{\partial \mathcal{B}} \boldsymbol{j} \cdot \boldsymbol{n} \, dA = Fc_{\text{max}} \, \text{C} - \text{rate} \int_{\mathcal{B}} 1 \, dV \quad (15)$$

into the active material. $\boldsymbol{n}$ denotes the inward surface normal and C-rate is the (dis-)charging rate given in 1/h. When the active material is parametrized via the smoothed boundary method, ψ denotes the local fraction of active material and the surface integral is replaced by a volume

integral

$$I \approx \int_{\mathcal{B}} j_N \, |\nabla\psi| \, \mathrm{d}V = F c_{\max} \, \mathrm{C-rate} \int_{\mathcal{B}} \psi \mathrm{d}V. \qquad (16)$$

to impose the boundary condition.

Data availability

The raw data and code which has been used to create Figs. 3 and 4 can be found on github [41]. Additional data from this study can be provided upon request.

Code availability

Code regarding methodology development and data fitting is published on https://github.com/daubners/multi-phase-sbm[41]. The software package Pace3D was used for the generation of multiphase-field simulation data sets. The software licence can be purchased from the Steinbeis Network (https://www.steinbeis.de) under the management of Britta Nestler and Michael Selzer under the heading "Material Simulation and Process Optimisation".

References

1. Kondrakov, A. O. et al. Anisotropic Lattice Strain and Mechanical Degradation of High- and Low-Nickel NCM Cathode Materials for Li-Ion Batteries. *J. Phys. Chem. C.* **121**, 3286–3294 (2017).
2. Xu, R., de Vasconcelos, L. S., Shi, J., Li, J. & Zhao, K. Disintegration of Meatball Electrodes for LiNi x Mn y Co z O2 Cathode Materials. *Exp. Mech.* **58**, 549–559 (2018).
3. Pfeiffer, L. F. et al. Layered P2-NaxMn3/4Ni1/4O2 Cathode Materials For Sodium-Ion Batteries: Synthesis, Electrochemistry and Influence of Ambient Storage. *Front. Energy Res.* **10**, 1–17 (2022).
4. Xu, Z. et al. Charge distribution guided by grain crystallographic orientations in polycrystalline battery materials. *Nat. Commun.* **11**, 83 (2020).
5. Müller, M., Schneider, L., Bohn, N., Binder, J. R. & Bauer, W. Effect of Nanostructured and Open-Porous Particle Morphology on Electrode Processing and Electrochemical Performance of Li-Ion Batteries. *ACS Appl. Energy Mater.* **4**, 1993–2003 (2021).
6. Daubner, S., Weichel, M., Hoffrogge, P. W., Schneider, D. & Nestler, B. Modeling Anisotropic Transport in Polycrystalline Battery Materials. *Batteries* **9**, 310 (2023).
7. Padhi, A., Nanjundaswamy, K. & Goodenough, J. Phospho-olivines as positive electrode materials for rechargeable lithium batteries. *J. Electrochem. Soc.* **144**, 1188 (1997).
8. Li, W., Reimers, J. N. & Dahn, J. R. In situ x-ray diffraction and electrochemical studies of Li1-xNiO2. *Solid State Ion.* **67**, 123–130 (1993).
9. de Biasi, L. et al. Phase Transformation Behavior and Stability of LiNiO2 Cathode Material for Li-Ion Batteries Obtained from In Situ Gas Analysis and Operando X-Ray Diffraction. *ChemSusChem* **12**, 2240–2250 (2019).
10. Lu, Z. & Dahn, J. R. In Situ X-Ray Diffraction Study of P2-Na2/3 Ni1/3 Mn2/3 O2. *J. Electrochem. Soc.* **148**, A1225 (2001).
11. Moreau, P., Guyomard, D., Gaubicher, J. & Boucher, F. Structure and Stability of Sodium Intercalated Phases in Olivine FePO4. *Chem. Mater.* **22**, 4126–4128 (2010).
12. Cogswell, D. & Bazant, M. Coherency strain and the kinetics of phase separation in LiFePO 4 nanoparticles. *ACS Nano* **6**, 2215–2225 (2012).
13. Daubner, S., Weichel, M., Schneider, D. & Nestler, B. Modeling intercalation in cathode materials with phase-field methods: Assumptions and implications using the example of LiFePO4. *Electrochim. Acta* **421**, 140516 (2022).
14. Hughes, T. J., Liu, W. K. & Zimmermann, T. K. Lagrangian-eulerian finite element formulation for incompressible viscous flows. *Computer methods Appl. Mech. Eng.* **29**, 329–349 (1981).
15. Joos, J., Carraro, T., Weber, A. & Ivers-Tiffée, E. Reconstruction of porous electrodes by FIB/SEM for detailed microstructure modeling. *J. Power Sources* **196**, 7302–7307 (2011).
16. Ender, M., Joos, J., Carraro, T. & Ivers-Tiffée, E. Three-dimensional reconstruction of a composite cathode for lithium-ion cells. *Electrochem. Commun.* **13**, 166–168 (2011).
17. Kench, S., Squires, I. & Cooper, S. TauFactor 2: A GPU accelerated python tool for microstructural analysis. *J. Open Source Softw.* **8**, 5358 (2023).
18. Bueno-Orovio, A., Pérez-García, V. M. & Fenton, F. H. Spectral Methods for Partial Differential Equations in Irregular Domains: The Spectral Smoothed Boundary Method. *SIAM J. Sci. Comput.* **28**, 886–900 (2006).
19. Yu, H.-C., Chen, H.-Y. & Thornton, K. Extended smoothed boundary method for solving partial differential equations with general boundary conditions on complex boundaries. *Model. Simul. Mater. Sci. Eng.* **20**, 075008 (2012).
20. Kockelkoren, J., Levine, H. & Rappel, W.-J. Computational approach for modeling intra- and extracellular dynamics. *Phys. Rev. E* **68**, 037702 (2003).
21. Fenton, F. H., Cherry, E. M., Karma, A. & Rappel, W.-J. Modeling wave propagation in realistic heart geometries using the phase-field method. *Chaos: Interdiscip. J. Nonlinear Sci.* **15**, 013502 (2005).
22. Li, X., Lowengrub, J., Ratz, A. & Voigt, A. Solving PDEs in complex geometries. *Commun. Math. Sci.* **7**, 81–107 (2009).
23. Reder, M., Hoffrogge, P. W., Schneider, D. & Nestler, B. A phase-field based model for coupling two-phase flow with the motion of immersed rigid bodies. *Int. J. Numer. Methods Eng.* **123**, 3757–3780 (2022).
24. Orvananos, B. et al. Architecture Dependence on the Dynamics of Nano-LiFePO4 Electrodes. *Electrochim. Acta* **137**, 245–257 (2014).
25. Yu, H. C., Choe, M. J., Amatucci, G. G., Chiang, Y. M. & Thornton, K. Smoothed Boundary Method for simulating bulk and grain boundary transport in complex polycrystalline microstructures. *Comput. Mater. Sci.* **121**, 14–22 (2016).
26. Yu, H.-C., Adler, S. B., Barnett, S. A. & Thornton, K. Simulation of the diffusional impedance and application to the characterization of electrodes with complex microstructures. *Electrochim. Acta* **354**, 136534 (2020).
27. Yu, H. C. et al. Designing the next generation high capacity battery electrodes. *Energy Environ. Sci.* **7**, 1760–1768 (2014).
28. Santoki, J. et al. Phase-field study of surface irregularities of a cathode particle during intercalation. *Model. Simul. Mater. Sci. Eng.* **26**, 065013 (2018).
29. Heo, T. W., Chen, L.-Q. & Wood, B. C. Phase-field modeling of diffusional phase behaviors of solid surfaces: A case study of phase-separating Li FePO4 electrode particles. *Computational Mater. Sci.* **108**, 323–332 (2015).
30. Hong, L., Liang, L., Bhattacharyya, S., Xing, W. & Chen, L. Anisotropic Li intercalation in a LixFePO4 nano-particle: A spectral smoothed boundary phase-field model. *Phys. Chem. Chem. Phys.* **18**, 9537–9543 (2016).
31. Qu, D. & Yu, H.-C. Multiphysics Electrochemical Impedance Simulations of Complex Multiphase Graphite Electrodes. *ACS Appl. Energy Mater.* **6**, 3468–3485 (2023).
32. Brosa Planella, F. et al. A continuum of physics-based lithium-ion battery models reviewed. *Prog. Energy* **4**, 042003 (2022).
33. Huang, Q. et al. Phase-field simulation for voltage profile of LixSn nanoparticle during lithiation/delithiation. *Computational Mater. Sci.* **220**, 112047 (2023).
34. Daubner, S. et al. Combined study of phase transitions in the P2-type NaXNi1/3Mn2/3O2 cathode material: experimental, ab-initio and multiphase-field results. *npj Computational Mater.* **10**, 75 (2024).

35. Hötzer, J. et al. The parallel multi-physics phase-field framework PACE3D. *J. Computational Sci.* **26**, 1–12 (2018).

36. Giudicelli, G. et al. 3.0 - MOOSE: Enabling massively parallel multiphysics simulations. *SoftwareX* **26**, 101690 (2024).

37. Mock, M., Bianchini, M., Fauth, F., Albe, K. & Sicolo, S. Atomistic understanding of the LiNiO2-NiO2 phase diagram from experimentally guided lattice models. *J. Mater. Chem. A* **9**, 14928–14940 (2021).

38. Zheng, S. et al. Microstructural Changes in LiNi 0.8 Co 0.15 Al 0.05 O 2 Positive Electrode Material during the First Cycle. *J. Electrochem. Soc.* **158**, A357–A362 (2011).

39. Das, H., Urban, A., Huang, W. & Ceder, G. First-Principles Simulation of the (Li-Ni-Vacancy)O Phase Diagram and Its Relevance for the Surface Phases in Ni-Rich Li-Ion Cathode Materials. *Chem. Mater.* **29**, 7840–7851 (2017).

40. Zhuang, D. & Bazant, M. Z. Theory of Layered-Oxide Cathode Degradation in Li-ion Batteries by Oxidation-Induced Cation Disorder. *J. Electrochem. Soc.* **169**, 100536 (2022).

41. Github repository with code used for this publication:. https://github.com/daubners/multi-phase-sbm.

42. Bouwman, P. J., Boukamp, B. A., Bouwmeester, H. J. M. & Notten, P. H. L. Influence of Diffusion Plane Orientation on Electrochemical Properties of Thin Film LiCoO[sub 2] Electrodes. *J. Electrochem. Soc.* **149**, A699 (2002).

43. Bazant, M. Z. Unified quantum theory of electrochemical kinetics by coupled ion-electron transfer. *Faraday Discuss.* **246**, 60–124 (2023).

44. Zhang, Y. et al. Lithium-ion intercalation by coupled ion-electron transfer https://chemrxiv.org/engage/chemrxiv-article-details/6653c53621291e5d1d57ad8b (2024).

45. Hess, A. et al. Determination of state of charge-dependent asymmetric Butler-Volmer kinetics for LixCoO2 electrode using GITT measurements. *J. Power Sources* **299**, 156–161 (2015).

46. Moelans, N., Blanpain, B. & Wollants, P. Quantitative analysis of grain boundary properties in a generalized phase field model for grain growth in anisotropic systems. *Phys. Rev. B - Condensed Matter Mater. Phys.* **78**, 024113 (2008).

47. Daubner, S., Hoffrogge, P. W., Minar, M. & Nestler, B. Triple junction benchmark for multiphase-field and multi-order parameter models. *Computational Mater. Sci.* **219**, 111995 (2023).

48. Gent, W. E. et al. Persistent State-of-Charge Heterogeneity in Relaxed, Partially Charged Li(1-x)Ni1/3Co1/3Mn1/3O2 Secondary Particles. *Adv. Mater.* **28**, 6631–6638 (2016).

49. Nguyen, T.-T. et al. Combining x-ray nano-ct and xanes techniques for 3d operando monitoring of lithiation spatial composition evolution in nmc electrode https://arxiv.org/abs/2307.08871 (2023).

50. Wang, J., Karen Chen-Wiegart, Y.-c, Eng, C., Shen, Q. & Wang, J. Visualization of anisotropic-isotropic phase transformation dynamics in battery electrode particles. *Nat. Commun.* **7**, 12372 (2016).

51. Fraggedakis, D. et al. A scaling law to determine phase morphologies during ion intercalation. *Energy Environ. Sci.* **13**, 2142–2152 (2020).

52. Chueh, W. C. et al. Intercalation Pathway in Many-Particle LiFePO 4 Electrode Revealed by Nanoscale State-of-Charge Mapping. *Nano Lett.* **13**, 866–872 (2013).

53. Li, Y. et al. Current-induced transition from particle-by-particle to concurrent intercalation in phase-separating battery electrodes. *Nat. Mater.* **13**, 1149–1156 (2014).

54. Deng, H. D. et al. Beyond Constant Current: Origin of Pulse-Induced Activation in Phase-Transforming Battery Electrodes. *ACS Nano* **18**, 2210–2218 (2024).

55. Newman, J. S. and Thomas-Alyea, K. E. *Electrochemical systems*, vol. 0 (J. Wiley, https://www.wiley.com/en-us/Electrochemical+Systems%2C+4th+Edition-p-9781119514602. edn. 2004).

56. Cahn, J. & Taylor, J. Surface motion by surface diffusion. *Acta Metall. et. Materialia* **42**, 1045–1063 (1994).

57. Hoffrogge, P. W. et al. Triple junction benchmark for multiphase-field models combining capillary and bulk driving forces. *Model. Simul. Mater. Sci. Eng.* **33**, 015001 (2025).

58. Plapp, M. Unified derivation of phase-field models for alloy solidification from a grand-potential functional. *Phys. Rev. E* **84**, 031601 (2011).

59. Choudhury, A. & Nestler, B. Grand-potential formulation for multicomponent phase transformations combined with thin-interface asymptotics of the double-obstacle potential. *Phys. Rev. E* **85**, 021602 (2012).

Acknowledgements

Author contributions

S.D. conceptualized the work and carried out the implementation and validation of the simulation code. S.D., M.R., D.S., and Q.H. all contributed to the formulation and validation of the MP-SBM method. S.D., A.E.C. and M.Z.B. formulated the electrochemical model; simulation studies and data visualization were carried out by S.D. and M.W.; D.S. and B.N. provided funding for the project. S.D., A.E.C., Q.H., M.Z.B. and B.N. wrote the manuscript. All authors read and approved the final manuscript.

Funding

Competing interests

The authors declare no competing interests.

Additional information

Supplementary information The online version contains supplementary material available at https://doi.org/10.1038/s41524-025-01707-1.

Correspondence and requests for materials should be addressed to Simon Daubner.

Reprints and permissions information is available at http://www.nature.com/reprints

Publisher's note Springer Nature remains neutral with regard to jurisdictional claims in published maps and institutional affiliations.